Space coding by gamma oscillations in the barn owl optic tectum

Devarajan Sridharan, Kwabena Boahen and Eric I. Knudsen

J Neurophysiol 105:2005-2017, 2011. First published 16 February 2011; doi:10.1152/jn.00965.2010

J Neurophysiol 105: 2005–2017, 2011.
First published February 16, 2011; doi:10.1152/jn.00965.2010.

Space coding by gamma oscillations in the barn owl optic tectum

Devarajan Sridharan,[1,2,3] Kwabena Boahen,[2,3] and Eric I. Knudsen[1,3]
Departments of [1]Neurobiology and [2]Bioengineering, [3]Program in Neurosciences, Stanford University School of Medicine, Stanford, California

Submitted 8 November 2010; accepted in final form 15 February 2011

Sridharan D, Boahen K, Knudsen EI. Space coding by gamma oscillations in the barn owl optic tectum. *J Neurophysiol* 105: 2005–2017, 2011. First published February 16, 2011; doi:10.1152/jn.00965.2010.—Gamma-band (25–140 Hz) oscillations of the local field potential (LFP) are evoked by sensory stimuli in the mammalian forebrain and may be strongly modulated in amplitude when animals attend to these stimuli. The optic tectum (OT) is a midbrain structure known to contribute to multimodal sensory processing, gaze control, and attention. We found that presentation of spatially localized stimuli, either visual or auditory, evoked robust gamma oscillations with distinctive properties in the superficial (visual) layers and in the deep (multimodal) layers of the owl's OT. Across layers, gamma power was tuned sharply for stimulus location and represented space topographically. In the superficial layers, induced LFP power peaked strongly in the low-gamma band (25–90 Hz) and increased gradually with visual contrast across a wide range of contrasts. Spikes recorded in these layers included presumptive axonal (input) spikes that encoded stimulus properties nearly identically with gamma oscillations and were tightly phase locked with the oscillations, suggesting that they contribute to the LFP oscillations. In the deep layers, induced LFP power was distributed across the low and high (90–140 Hz) gamma-bands and tended to reach its maximum value at relatively low visual contrasts. In these layers, gamma power was more sharply tuned for stimulus location, on average, than were somatic spike rates, and somatic spikes synchronized with gamma oscillations. Such gamma synchronized discharges of deep-layer neurons could provide a high-resolution temporal code for signaling the location of salient sensory stimuli.

multimodal spatial localization; local field potential; superior colliculus; multimodal oscillations

VISUAL AND AUDITORY STIMULI have been shown to evoke oscillations in the local field potential (LFP) in numerous forebrain areas in mammals (Brosch et al. 2002; Henrie and Shapley 2005). LFP oscillations in the frequency range of 25–140 Hz are referred to as gamma-band oscillations (Pesaran et al. 2002; Canolty et al. 2006; Ray et al. 2008a; Colgin et al. 2009; Khawaja et al. 2009; Vianney-Rodrigues et al. 2011). In many forebrain areas, gamma-band oscillations of the LFP are modulated dramatically in amplitude when an animal attends to a stimulus (Fries et al. 2001; Fries et al. 2008; Khayat et al. 2010). Within the gamma-band, the lower (25–90 Hz) and higher (90–140 Hz) ranges are thought to reflect different underlying mechanisms (Buzsaki et al. 1992; Traub et al. 1996; Traub et al. 1999a,b; Brunel and Wang 2003; Traub et al. 2003; Sohal et al. 2009). Low gamma oscillations show narrow tuning to a variety of stimulus features, including contour orientation, speed, direction, and contrast (Kayser and König 2004; Henrie and Shapley 2005; Liu and Newsome 2006; Berens et al. 2008). Although the stimulus-dependent properties of gamma oscillations have been characterized extensively in the mammalian forebrain, gamma oscillations in other brain areas or in other classes of animals are less well studied.

Here we report on gamma-band LFP oscillations in the avian optic tectum (OT), the homolog of the mammalian superior colliculus (SC), a structure involved in multimodal spatial localization and the control of spatial attention (Stein and Meredith 1993; McPeek and Keller 2004; Muller et al. 2005; Winkowski and Knudsen 2006; Winkowski and Knudsen 2007; Lovejoy and Krauzlis 2010). The OT and SC are multilayered structures that contain mutually aligned, topographic maps of visual and auditory space (Knudsen 1982; Middlebrooks and Knudsen 1984). The superficial layers (Fig. 1) receive direct visual input as well as input from primary and secondary visual areas in the forebrain, and they project to visual nuclei in the thalamus (Karten et al. 1973; Bravo and Pettigrew 1981; Wild 1989; Berman and Wurtz 2010; Lyon et al. 2010). Lesions of the superficial layers lead to deficits in visual discrimination behaviors (Casagrande et al. 1972; Casagrande and Diamond 1974). On the other hand, the deep layers (Fig. 1) receive multimodal sensory inputs as well as movement-related information, and they project to thalamic, midbrain, and pontine nuclei involved in attention and orienting behaviors (Stein and Meredith 1993; Karten et al. 1997; May 2006; Fedtsova et al. 2008). Lesion or inactivation of the deep layers causes deficits in attention and orienting behaviors (Raczkowski et al. 1976; Knudsen et al. 1993; Lovejoy and Krauzlis 2010).

The functional properties of gamma-band LFP oscillations in the OT are not known (Neuenschwander and Varela 1993). Although units in the mammalian SC have been shown to discharge synchronously with gamma periodicity in response to salient visual stimuli (Brecht et al. 2001), the stimulus-dependent properties of this oscillatory activity have not been studied. We show that gamma oscillations in the avian OT can be evoked by either visual or auditory stimuli and that they depend on the location and strength of these stimuli. Moreover, the oscillations exhibit distinctive functional properties in the superficial and deep layers of the OT. Finally, somatic spikes in the deep layers synchronize with gamma oscillations and could, therefore, contribute to information processing in the OT by providing a high-resolution synchrony code for signaling stimulus location. Such a characterization of the space-coding properties of gamma-band oscillations in the avian OT lays the foundation for understanding the role of these oscillations in spatial localization and spatial attention across different classes of vertebrate animals.

Address for reprint requests and other correspondence: D. Sridharan, Dept. of Neurobiology, 259 Campus Dr. West, D255, Stanford, CA, 94305 (e-mail: dsridhar@stanford.edu).

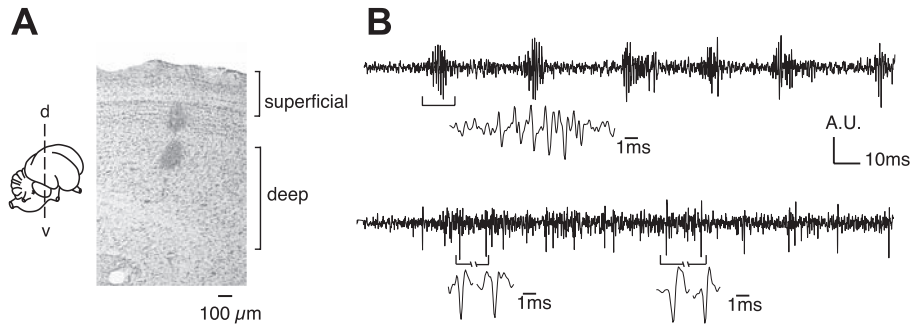

Fig. 1. Anatomical and physiological landmarks for the superficial and deep layers of the optic tectum (OT). Superficial layers (1–10) exhibited characteristic bursty spiking activity (upper lesion). Deep layers (12–13) exhibited single, somatic spikes that discharged regularly; bursty activity was negligible or undetectable (lower lesion). Recordings were not made in layer 11 (between the lesions). A.U., arbitrary units; d, dorsal; v, ventral.

MATERIALS AND METHODS

Animals. Three adult barn owls were used in this study. Methods for bird care and surgery were approved by the Stanford University Institutional Animal Care and Use Committee and were in accordance with the National Institutes of Health and the Society for Neuroscience guidelines for the care and use of laboratory animals. Surgical and experimental procedures have been described previously (Mysore et al. 2010). Owls were lightly tranquilized and maintained in a passive state on a mixture of nitrous oxide and oxygen (45:55) for the duration of the experiment.

Neurophysiology. Epoxy-coated tungsten microelectrodes (0.5–1 MOhm at 1 kHz; FHC, Bowdoin, ME; ALA Scientific instruments, Farmindale, NY) were used to record LFPs and single and multiple units in the superficial layers (1–9) and deep layers (12–15) of the OT. Recording sites were assigned to the superficial layers if they exhibited large amplitude bursting spike responses and to the deep layers if they exhibited regularly spiking (nonbursting) units (Fig. 1). To verify these physiological markers, lesions were made at transition sites, and the locations of the lesions were reconstructed in Nissl-stained sections (DeBello and Knudsen 2004). Raw field signal, sampled at 25 kHz, was buffered and stored for offline analysis; the preamplifier (Medusa; Tucker-Davis Technologies, Alachua, FL) had a high-pass cutoff of 2.2 Hz, and a low-pass cutoff of 7.5 kHz (3 dB corner, 1st order, 6 dB per octave). Following band-pass filtering (300 Hz to 4.7 kHz) to isolate spike activity, spike times were recorded as the first instant of time (within a fixed time window) the high-frequency signal amplitude exceeded a visually determined threshold that was determined post hoc to be four to five standard deviations of the mean at baseline. Spike times were computed and stored online using Tucker-Davis hardware (RA-16) controlled by customized Matlab (2007a; The MathWorks, Natick, MA) software. Spikes and LFPs were recorded from 1,000 ms before stimulus onset until 1,000 ms after stimulus offset.

Stimuli. Visual and auditory stimuli were presented for durations of either 250 or 350 ms. The number of trials repeated for a given stimulus parameter configuration ranged from 10 to 15, and interstimulus intervals were 2.5 s.

Visual stimuli were 1–2° radius, negative-contrast (black on a gray background) dots that were typically stationary. For a few sites, spike responses to the stationary dot habituated strongly, and for these sites moving (speed: 15–20°/s) dots were used. These were created using customized Matlab software (J. Bergan, Harvard University, Cambridge, MA) and presented (Mitsubishi XD300U projector) on a calibrated tangent screen at a distance of 35 cm from the eyes. The owl was positioned so that the visual axes were in the horizontal plane aligned with 0° elevation and 0° azimuth of the screen. All locations are given in double pole coordinates of azimuth, relative to the midsagittal plane, and elevation, relative to the visual plane.

Auditory stimuli were noise bursts (2–10 kHz, 0 ms rise/fall times, 10–20 dB above unit threshold). Auditory stimuli were generated using customized Matlab software interfaced with Tucker Davis Technologies hardware (RP2). Sounds were filtered with head-related transfer functions from a typical barn owl (Witten et al. 2010) and delivered binaurally through matched earphones (ED-1914; Knowles Electronics, Itasca, IL) coupled to damping assemblies (BF-1743) inserted into the ear canals ~5 mm from the eardrums. The amplitudes of the two earphones were equalized to within ± 2 dB.

Spatial tuning curves and contrast-response functions. Spatial tuning curves were measured by systematically changing the azimuth or elevation of the visual stimulus, in steps of 2–4°. Azimuthal tuning curves were measured at the best elevation (center of the weighted average of spike responses) for the site and vice versa for elevational tuning curves (Mysore et al. 2010).

Visual contrast-response functions were measured by altering the contrast of the visual stimulus from full negative contrast (100%: black on gray background) to null contrast (0%: gray on gray background) in steps of 10%. Luminance was measured using a photodiode. Contrast was calculated as the percentage change in luminance from an arbitrary gray baseline (corresponding to the midpoint of the grayscale in Matlab). Contrast-response functions were acquired at the best azimuth and best elevation for the site.

LFP analysis. We removed 60-Hz line noise and its second harmonic (120 Hz) from the recording using the *rmlinesc* function, available from the Chronux toolbox (http://www.chronux.org). To remove spikes from the field recording, previous studies have either *1*) subtracted a mean spike waveform at each occurrence of the spike in the field recording (Pesaran et al. 2002) or *2*) linearly interpolated the field signal in a fixed time window around the occurrence of each spike in the field recording (Manning et al. 2009). Because our deep layer recordings were typically multiunits, subtracting a mean spike waveform would introduce artifacts in the field recordings when the different units had substantially different waveforms. Also, because spikes recorded in the superficial layers occurred in 2–4-ms bursts that were tightly phase-locked with the oscillation, interpolating around these bursts of spikes (second procedure) would have substantially degraded the oscillatory field signal. Hence, to remove spikes from the field recording, we adopted the following procedure: we bandpass filtered the data between 300 Hz and 4.7 kHz and then subtracted this signal from the original signal to yield the remnant signal with the low frequencies (RLF signal). Spikes in bandpass-filtered data were removed by linearly interpolating the field recording in a ±2-ms window surrounding each spike (or burst). This trace was then added back to RLF signal to yield the complete spike-subtracted signal. The denoised and spike-subtracted data were then low-pass filtered at 200 Hz and downsampled at 1 kHz to make the data computationally tractable, using the *resample* function in Matlab. This is the LFP signal that was subjected to spectral analysis. Examples of recordings in the superficial and deep layers before and after this spike-subtraction procedure, as well as the LFP, are shown in Supplemental Fig. S1; supplemental material for this article is available online at the *Journal of Neurophysiology* website. All filters used were zero-phase Butterworth filters designed to have no more than 0.1 dB of attenuation in the passband and at least 3 dB of attenuation in the stop band. Filters were designed using the *buttord* and *butter* functions, and zero-phase filtering was done with the *filtfilt* function, in Matlab.

Spectral analysis was performed using multitaper spectral estimation implemented in the Chronux toolbox (Mitra and Bokil 2008). For

each stimulus configuration (location, contrast, modality), evoked power was calculated by averaging the evoked response across trials before time-frequency analysis. The evoked power constitutes the stimulus-locked part of the oscillations. The induced power was then computed by first performing time-frequency analysis for each trial, averaging the spectra, and then subtracting the evoked power. This procedure removes stimulus-locked contributions to the oscillations from the spectral profile.

Spectrograms were computed using a moving window of length 300 ms (shifted in 5-ms increments) and 3 tapers (K = 3), permitting a time-bandwidth product of 2 (TW = 2) and a frequency resolution of ~6 Hz. Because raw spectral power in the LFP decreases exponentially at higher frequencies, we plot the R-spectrogram to reveal the frequencies of induced gamma activity. The R-spectrogram was computed by normalizing the induced power in the spectrogram at each frequency by the power in that frequency in a baseline window extending 50 ms to 350 ms before stimulus onset. Similar ratio spectra with induced power normalized on a frequency-by-frequency basis have been reported in previous studies (Henrie and Shapley 2005; Fries et al. 2008).

For R-spectra shown in Fig. 3, spectra were computed in a response window that excluded onset transients. For visual stimuli, this window was 100 ms following stimulus onset (as the earliest latency of visual responses was typically ~60 ms) to 100 ms following stimulus offset. For auditory stimuli, the window was 35 ms following stimulus onset (as the earliest latency of auditory responses was ~8 ms following stimulus onset) to 35 ms following stimulus offset. Oscillations typically persisted even after stimulus offset, and we did not detect strong offset transients in the responses. However, we repeated the analysis in narrower response windows that terminated at stimulus offset and found results similar to those reported here.

For computing R-spectra, induced LFP power was normalized to its baseline value for each frequency (averaged across trials). R-spectra were then averaged across sites (Henrie and Shapley 2005). For Supplemental Fig. S2 R-spectra were normalized by the maximum power within the gamma-band to facilitate comparing frequencies of peak induced gamma power in superficial and deep layer sites on the same axis.

Comparing spike and LFP tuning, and contrast response. To compare tuning widths between multiunits and LFP, we computed the percentage change in spike rates and in low gamma LFP power (25–90 Hz) (TW = 2, K = 3) relative to baseline (same time windows as were used for the R-spectra). We fitted the tuning curves with a cubic spline and computed tuning widths as the width of cubic spline fits at half of the maximum (half-max) value. Spike or LFP tuning curves for which the half-max width could not be calculated (typically because of insufficient sampling of space on either side of the receptive field center) were not included in the analysis.

Discrimination index (d′) was computed for spike rates and LFP power spatial tuning curves as the difference in means divided by the joint standard deviation: $(\mu_1 - \mu_2)/\sqrt{(\sigma_1 \cdot \sigma_2)}$ where μ_1 is the mean firing rate at spatial location X_1, μ_2 is the mean firing rate at spatial location X_2, and σ_1 and σ_2 are the standard deviations of the firing rates at X_1 and X_2, respectively. This index, also called the standard separation (Sakitt 1973), has been used as a measure of spatial acuity both at the neural and behavioral levels (Bala et al. 2003; Bala et al. 2007; Winkowski et al. 2008). Contrast-response functions were fit with logistic sigmoidal functions (of the form: $A/[B + e^{C*x}]$). Transition ranges were computed as the range of contrasts over which the fitted sigmoid changed from 10% to 90% of its range of change, and the 50% contrast point was the contrast at which the fitted sigmoid reached 50% of its full range. For display purposes, tuning curves and contrast-response functions for spikes and LFPs were normalized to their maximum values. Several analyses were repeated with LFP root-mean-squared (rms) amplitude in the place of LFP power, where LFP rms amplitude was calculated as the square root of LFP power.

Fisher information represents knowledge about the stimulus contained in the neural responses. Fisher information was computed as $I_{Fisher}(s) = \sum_r P(r|s) \{^d/_{ds} [\log_e P(r|s)]\}^2$, where $I_{Fisher}(s)$ is the Fisher information associated with a particular stimulus s (measured in degrees from the receptive field center); r represents response values (measured as percentage change over baseline spike rate or gamma LFP power); P(r|s) represents the probability of observing response value r given stimulus s, and $\log_e$ is the natural logarithm function (Quian Quiroga and Panzeri 2009). For computing P(r|s), r-values were binned in 2.5% increments, and s-values were binned in 5° increments. Fisher information for the population response was computed as the sum of the Fisher information across the population of sites by treating responses acquired at different sites as independent observations (Seung and Sompolinsky 1993). Fisher information was computed after centering the tuning curve for each site at its maximum value and was normalized by the number of sites in the population (Supplemental Fig. S3).

Spike-field coherence. Spike-field coherence (SFC) was computed using the Chronux toolbox. The mean evoked LFP response across trials was subtracted from the single-trial responses to remove stimulus-locked contributions to the oscillations. Coherograms (Fig. 9, *A* and *B*) were computed using a moving window of length 300 ms shifted in 5-ms increments and 7 tapers (K = 7; TW = 4, frequency resolution of ~13 Hz) using the Chronux toolbox. Coherences (plotted in Fig. 9*C*, Supplemental Figs. S4 and S5) were calculated with bandwidth, W = 25 Hz (Fries et al. 2008; Gregoriou et al. 2009). To verify that the coherences were not a result of stimulus-locked oscillations, LFP and spike responses were matched randomly across trials, and the resulting coherences were calculated (Supplemental Fig. S4*B*).

Spikes in the superficial layers occurred as bursts of 4–8 spikes (Fig. 1). Because each spike in a burst occurred separated from its neighbors by a typical, fixed interspike interval of 2–3 ms, consistent locking of one of the spikes in the burst to LFP oscillation phase automatically meant that all of the other spikes in the burst were similarly phase locked. Hence, SFC computed with only the first spike of each burst sufficed to test whether spike times in the superficial layers were phase locked to gamma oscillations, and all SFC values reported are based on this analysis (Fig. 9, A and C, Supplemental Fig. S4). In addition, we reanalyzed superficial layer SFC including all spikes in the burst; although the overall SFC magnitude was higher, the relative magnitude of the coherence at different frequencies remained the same, in line with expectations (Supplemental Fig. S5).

RESULTS

Multimodal stimuli evoke gamma LFP oscillations across tectal layers. Stimulus-driven LFP responses were recorded at several locations along an electrode penetration through the OT. We refer to OT layers 1–10 as the superficial layers; superficial layer recordings were typically made in layers 4–8. The superficial layers were readily identified neurophysiologically by the presence of large-amplitude bursting spikes (Fig. 1). These bursting spikes are likely to include axonal spikes from neurons located in the cholinergic nucleus isthmi pars parvocellularis (Ipc; see DISCUSSION). We refer to OT layers 12–15 as the deep layers; deep layer recordings were typically made in layers 12–13. Recordings in the deep layers were dominated by large somatic spikes, and bursting activity was weak or not measurable. Previous studies refer to these as the intermediate and deep layers (Mysore et al. 2010). Recordings were not made in layer 11, a cell-sparse layer.

Robust LFP responses were evoked by centering either a visual or an auditory stimulus (see MATERIALS AND METHODS) in the spike-receptive field for the recording site. Examples of

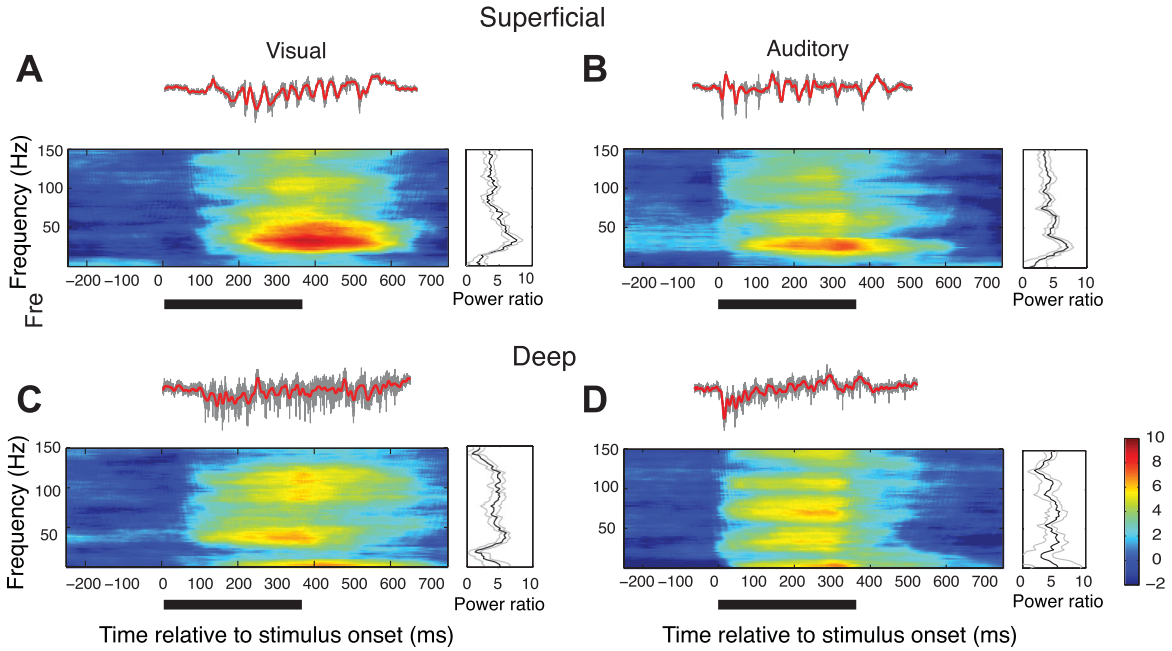

Fig. 2. Gamma oscillations evoked by visual and auditory stimuli in the superficial and deep layers. Local field potential (LFP) responses to a vertically moving dot (speed: 15°/s, *left*) or broadband noise bursts (*right*). The stimuli were presented at the center of the receptive field of the site. Gray traces show unfiltered activity; red traces show LFP (see MATERIALS AND METHODS). *A*: average R-spectrogram measured in the superficial layers. Power relative to baseline (in dB, see MATERIALS AND METHODS) is plotted as a function of frequency and time relative to stimulus onset, averaged over 10 repetitions of the stimulus. Color bar indicates power relative to baseline (in dB). The dark bar under the spectrogram indicates duration of stimulus presentation (onset at 0 ms). *Right*: average induced LFP power (R-spectrum) at 260 ms. Gray lines indicate standard error across repetitions. *B*: same as in *A*, for an auditory stimulus. *Right*: average induced LFP power at 180 ms (the earlier time for computing induced power is on account of the earlier onset of the auditory response). *C*: same as in *A*, for a site recorded in the deep layers. *D*: same as in *C*, for an auditory stimulus.

LFP responses, recorded in the superficial and deep layers, are shown in Fig. 2. LFP responses typically persisted for roughly 100 ms following stimulus offset. In the superficial layers, the LFP evoked by a visual stimulus showed induced power across the gamma-band with a prominent peak in the low-gamma band (25–90 Hz) (Fig. 2*A*, R-spectrogram, see MATERIALS AND METHODS). With the electrode at the same site, an auditory noise burst presented from the same location in space evoked an LFP with a similar induced spectral profile, dominated by low-gamma power (Fig. 2*B*). When the electrode was advanced into the deep layers, the power spectrum of the LFP changed; visual and auditory stimuli from the same locations in space evoked LFPs with induced power in both low and high (90–140 Hz) gamma-bands (Fig. 2, *C* and *D*). These characteristics also applied to the population-averaged LFPs from the superficial and deep layers (Fig. 3). At any given site, visual and auditory stimuli evoked LFPs with similar induced power spectra. Average R-spectra (see MATERIALS AND METHODS) for the LFPs evoked by visual and auditory stimuli in the superficial layers were dominated by induced power in the low-gamma band (Fig. 3*A*, $n = 11$). On the other hand, average R-spectra for LFPs evoked by visual and auditory stimuli in the deep layers showed induced power that was distributed across the gamma-band (Fig. 3*B*, $n = 17$). The magnitudes of population-averaged R-spectra were comparable across layers except for a large peak at ~40 Hz in the superficial layers (Fig. 3).

Subsequent analyses of LFP oscillations are based on visually induced low-gamma (25–90 Hz) responses (Fig. 3, gamma frequency range as in Pesaran et al. 2002; Henrie and Shapley, 2005; Katzner et al. 2009; Burns et al. 2010). We decided not to analyze the high-gamma (90–140 Hz) band separately because in our recordings spectral power decreased exponentially at higher frequencies, making reliable estimation of signal power in the high-gamma band difficult. In addition, there is greater potential for spike waveforms to contaminate

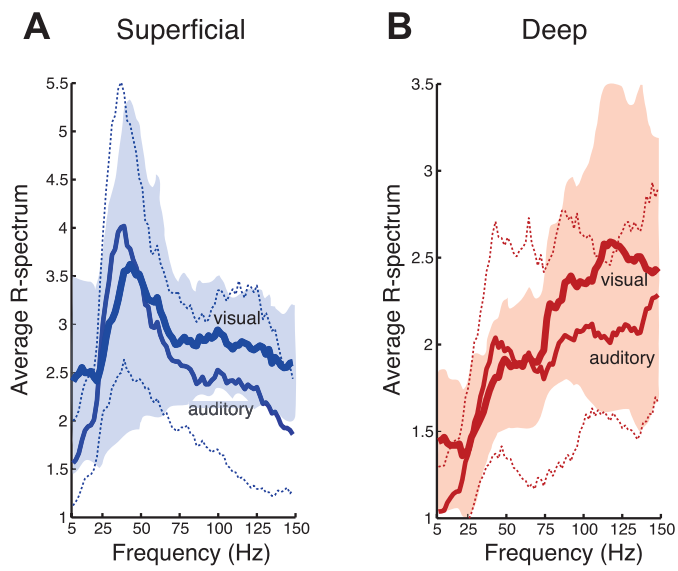

Fig. 3. Power spectra of LFP responses to visual and auditory stimuli in the superficial and deep layers. *A*: average R-spectra of induced LFP power in the superficial layers. An R-spectrum value of 1 indicates power at baseline. Thick line: visual responses; thin line: auditory responses ($n = 11$). Shaded region: 95% confidence intervals for R-spectra induced by visual stimuli. Region between dotted lines: 95% confidence intervals for R-spectra induced by auditory stimuli. *B*: average R-spectra as in *A*, for induced LFP power in the deep layers ($n = 17$).

the LFP in the high-gamma band (Colgin et al. 2009; Zanos et al. 2011; see DISCUSSION). For the results reported subsequently, visually evoked LFP responses were recorded at additional superficial (n = 25, total) and deep layer sites (n = 32, total). Average R-spectra for the population of sites used in the analyses are reported in Supplemental Fig. S2.

Spatial tuning of gamma oscillations. To understand how induced gamma LFP power depended on stimulus location we presented visual stimuli at different locations in azimuth and elevation in an interleaved fashion. In both superficial and deep layers, induced gamma LFP power peaked sharply when the stimulus was centered in the spike-receptive field and decreased systematically as the stimulus was moved away from the center (Fig. 4, *A* and *D*). Tuning shifted systematically with recording site location across the OT, following the well-known map of space based on unit-receptive fields (Knudsen 1982); frontal locations were represented rostrally, peripheral locations caudally, upper locations dorsally, and lower locations ventrally. The sharpness of the spatial tuning, in azimuth or elevation, of gamma LFP responses was similar in the superficial and deep layers (width at half-max: superficial layers = 9.04 ± 0.85°, n = 29, deep layers = 9.35 ± 0.76°, mean ± SE, n = 45, P = 0.90, Mann-Whitney U-test).

We compared the spatial tuning of spikes with the spatial tuning of LFPs recorded at the same sites. The centers of LFP spatial tuning were closely aligned with centers of spike tuning (Figs. 4 and 5*A*). The sharpness of spatial tuning, measured as width at half-max, was similar for spikes and LFPs in the superficial layers (Figs. 4*C*, and 5*B*, blue circles, width at half max, LFP = 9.04 ± 0.85°, spikes = 9.05 ± 0.50°, mean ± SE, P = 0.99; n = 28) but broader for spikes than for LFPs in the deep layers (Figs. 4*F* and 5*B*, red circles, width at half-max, LFP = 9.35 ± 0.76°, spikes = 12.59 ± 1.12°, mean ± SE, $P < 0.001$, n = 42, Wilcoxon signed-rank test). Particularly, for almost all sites at which the spatial width at half-max for spikes exceeded 10°, width at half-max for gamma LFP tuning

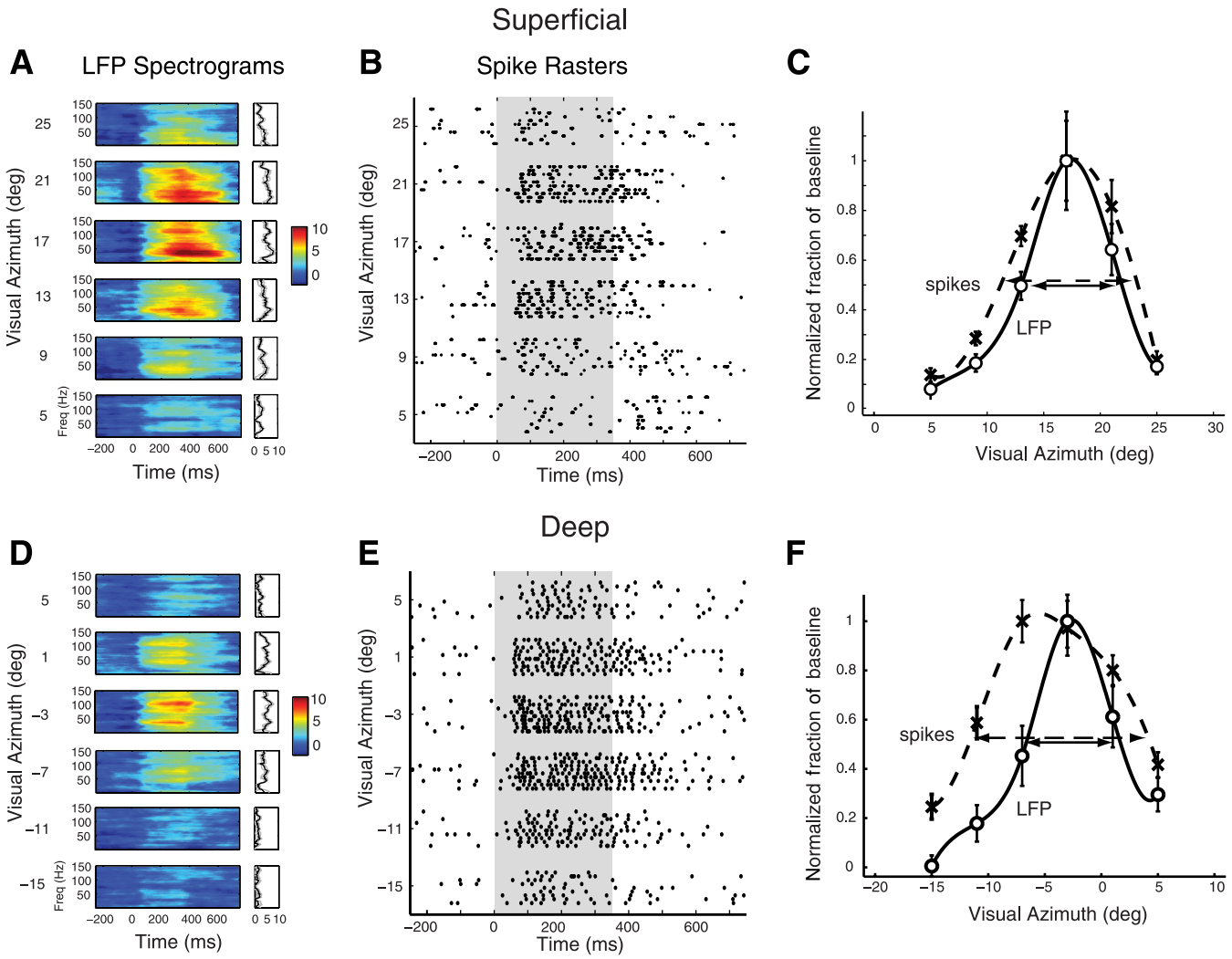

Fig. 4. Spatial tuning of induced gamma LFP power and spike rates at individual sites in the superficial and deep layers. *A*: R-spectrograms showing the modulation of gamma LFP power for a representative site in the superficial tectum when a visual stimulus was presented at different azimuthal locations at the best elevation of the site (as measured from spike rates) for the site. Other conventions are described in Fig. 2. *B*: spike rasters, recorded at the same site as in *A*, showing tuning in spike rates to stimulus location. Shaded gray area corresponds to stimulus presentation. Note that spikes occurred in bursts of 4–5 spikes. *C*: gamma LFP tuning curve (○), and cubic-spline fit (solid line), as well as spike rate tuning curve (crosses), and cubic spline fit (dashed line). Each tuning curve was normalized to its maximum so that the full-width at half-max occurred at an ordinate value of 0.5. *D*: same as in *A*, for a site recorded from the deep layers. *E*: same as in *B*, for the same deep layer site as in *D*. *F*: same as in *C*, for the same deep layer site as in *D*.

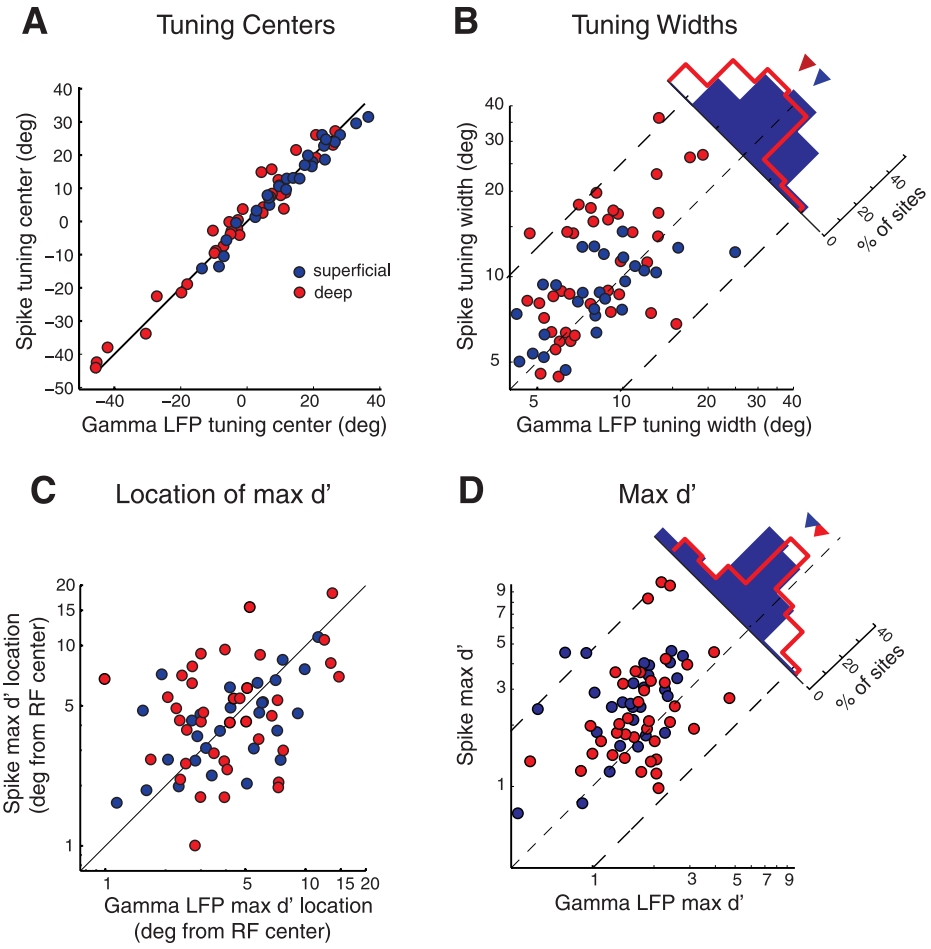

Fig. 5. Population summary comparing the spatial tuning of induced gamma LFP and spikes. Spatial tuning was measured in azimuth and/or elevation (see MATERIALS AND METHODS). *A*: spatial tuning centers for gamma LFP power (*x*-axis) and spike rates (*y*-axis) at sites in the superficial (blue) and deep (red) tectal layers. *B*: spatial tuning widths at half-max of gamma LFP power (*x*-axis) and spike rates (*y*-axis). The histogram shows the distribution of the ratio of LFP to spike tuning widths for the superficial and deep sites. Inverted triangles: medians of the respective distributions. *C*: locations of maximal discrimination index values (max d′) for gamma LFP power (*x*-axis) and spike rates (*y*-axis) measured relative to the center of the receptive field (RF). *D*: max d′ values for gamma LFP power (*x*-axis) and spike rate (*y*-axis) tuning curves. Other conventions are the same as in *B*. All data are drawn from the same population of tuning curves in the superficial ($n = 28$) and deep ($n = 42$) layers.

was narrower (Fig. 5*B*). Because computing LFP power involves a nonlinearity (squaring the amplitude), we tested whether measuring LFP tuning widths on the basis of rms amplitude would eliminate the relative narrowness of LFP tuning (see MATERIALS AND METHODS). Although LFP tuning based on rms amplitude was wider than that based on power, rms tuning was comparable to spike tuning in the superficial layers and remained narrower than spike tuning in the deep layers ($P = 0.004$, Wilcoxon signed-rank test). These results suggest that gamma LFPs are tuned at least as narrowly as spikes in the superficial layers and more narrowly than spikes in the deep layers.

Given the sharp spatial tuning of LFP power, we tested whether changes in LFP power discriminated between adjacent stimulus locations with a resolution comparable to that of spikes. Maximal discrimination (max d′ for adjacent stimuli; see MATERIALS AND METHODS) typically occurred on the flanks of the tuning curves for both spikes and LFPs (Fig. 5*C*). The distances of the max d′ locations from receptive-field center were tightly correlated between spikes and LFP in the superficial layers (Fig. 5*C*, blue, $R^2 = 0.39$, $P < 0.001$) but uncorrelated in the deep layers (Fig. 5*C*, red, $R^2 = 0.07$, $P = 0.11$). Spikes consistently exhibited greater max d′ values than did LFP power (superficial layers: mean max d′ spikes = 2.39 ± 0.20, LFP = 1.32 ± 0.11, mean ± SE, $P < 0.001$, $n = 28$, Fig. 5*D*, blue data; deep layers: mean max d′ spikes = 2.41 ± 0.33, LFP = 1.54 ± 0.11, mean ± SE, $P < 0.001$, $n = 42$, Fig. 5*D*, red data, Wilcoxon signed-rank test). These trends remained valid after recalculating d′ on the basis of LFP rms amplitude. Thus, on average, spike rates discriminated stimulus locations at their receptive field flanks with higher resolution than did gamma LFP power in both the superficial and deep layers.

Next, we compared the spatial information content of spikes and LFPs using the Fisher information metric (see MATERIALS AND METHODS). The inverse of the Fisher information represents a lower bound on the mean-squared decoding error obtainable with any unbiased decoder (Quian Quiroga and Panzeri 2009). We found that the Fisher information in the population of neurons was higher for spike rates (Supplemental Fig. S3 solid) than gamma LFP power (Supplemental Fig. S3 dashed) across the range of stimuli presented to the population, both for superficial ($n = 28$) and deep ($n = 42$) layer sites. Furthermore, Fisher information for both spike rates and gamma LFP power peaked on the flanks of the population tuning curve (Supplemental Fig. S3). Thus spike rates contained greater information regarding spatial locations than did gamma LFP power, indicating a potentially higher accuracy of decoding stimulus spatial location with spike rates.

Effect of visual contrast on gamma oscillations. To understand how induced LFP power was affected by stimulus strength, we presented stimuli of different visual contrasts at the center of the receptive field for a subset of recording sites (13 superficial, and 16 deep layer sites). An example of the effects observed in the superficial layers is shown in Fig. 6*A*.

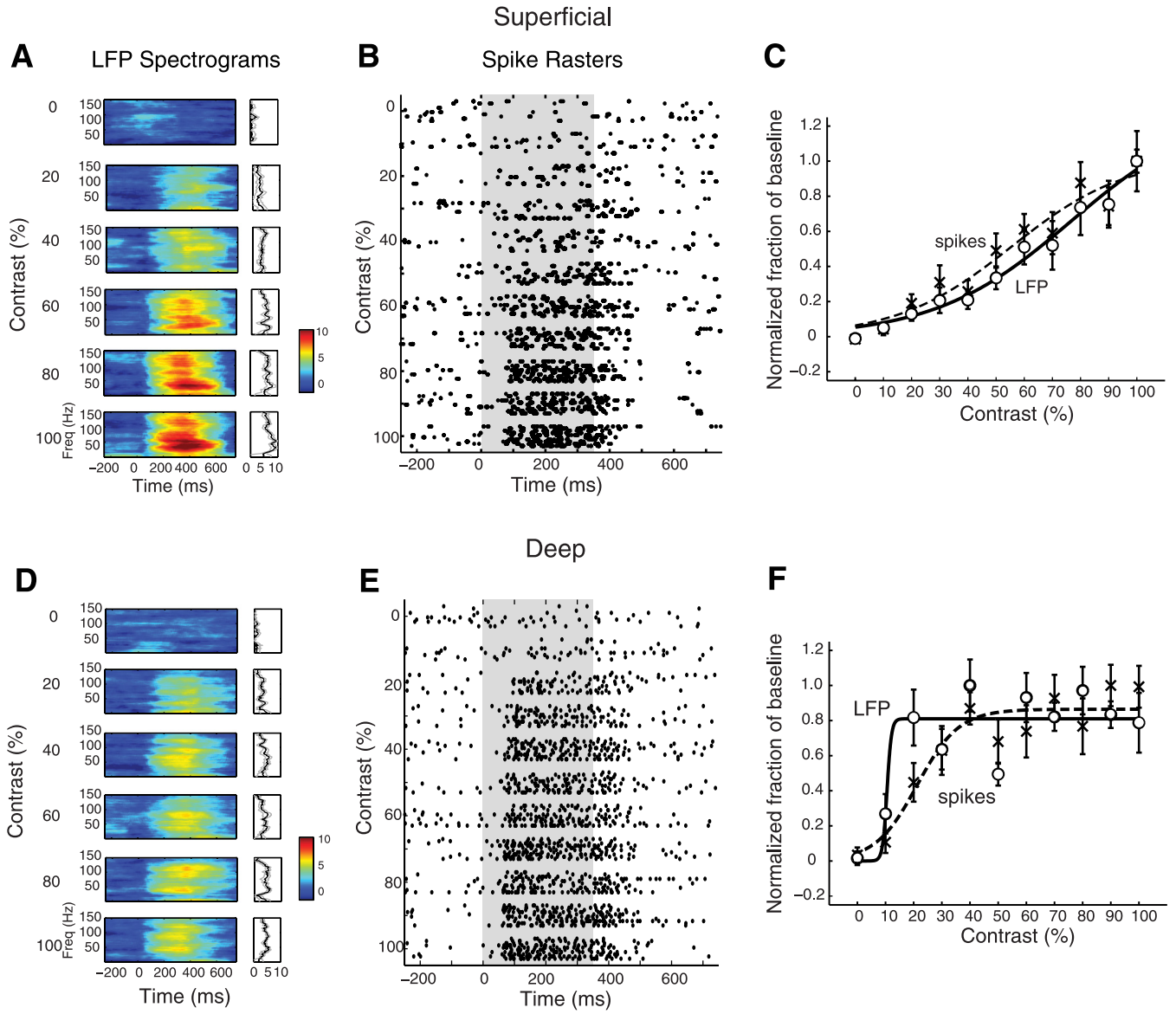

Fig. 6. Contrast-response functions for induced gamma LFP power and spike rates at individual sites in the superficial and deep layers. *A*: R-spectrogram for a representative superficial layer site showing the increase in gamma LFP power in response to increasing visual stimulus contrast presented at the center of the receptive field. Other conventions are as in Fig. 4. *B*: spike rasters showing spike responses recorded at the same superficial site as in *A*. Other conventions are as in Fig. 4. *C*: gamma LFP contrast-response (○) and sigmoidal fit (solid line), as well as spike rate contrast-response (crosses) and sigmoid fit (dashed line). Each curve was normalized to its maximum to facilitate comparison of the respective transition ranges (the contrast range over which gamma LFP power changed from 10% to 90% of its maximum range). *D*: same as in *A*, for a representative site in the deep layers. *E*: same as in *B*, for the same deep layer site as in *D*. *F*: same as in *C*, for the same deep layer site as in *D*.

Gamma power at all frequencies increased gradually and systematically with contrast over a wide range of contrasts. Similar trends were observed in the population of superficial layer sites (Fig. 7*A*). On the other hand, contrast-response functions in the deep layers typically exhibited a different characteristic. As exemplified by the site shown in Fig. 6*D*, LFP power usually increased abruptly with increasing contrast at low visual contrasts, then remained constant to further increases in contrast. The population of deep layer sites exhibited similar trends (Fig. 7*B*).

To quantify these trends, we computed the abruptness of the increase in LFP power with increasing stimulus contrast as the range of contrasts (transition range) over which LFP power increased from 10% to 90% of its full range. In the superficial layers, the median [95% confidence interval] transition range was 60.9% [32.8–74.4%] (Fig. 7*C*, blue arrowhead). In the deep layers, the median transition range was 17.4% [5.4−39.5%], more than three times as sharp (Fig. 7*C*, red arrowhead). The visual contrast at which LFP power reached the center of its full transition range is referred to as the 50% contrast. In the superficial layers, the 50% contrast was 48.4 [39.9−66.4] %, essentially centered in the range of tested contrasts (Fig. 7*D*, blue arrowhead). In the deep layers, the average 50% contrast was 22.9 [18.7–34.0] %, near the low end of the contrast range (Fig. 7*D*, red arrowhead). The superficial and deep layer distributions of transition ranges (Fig. 7*C* blue vs. red) and 50% contrasts (Fig. 7*D*, blue vs. red) were significantly different from each other ($P < 0.005$, $n = 13$ superficial and 16 deep, Mann-Whitney *U*-test).

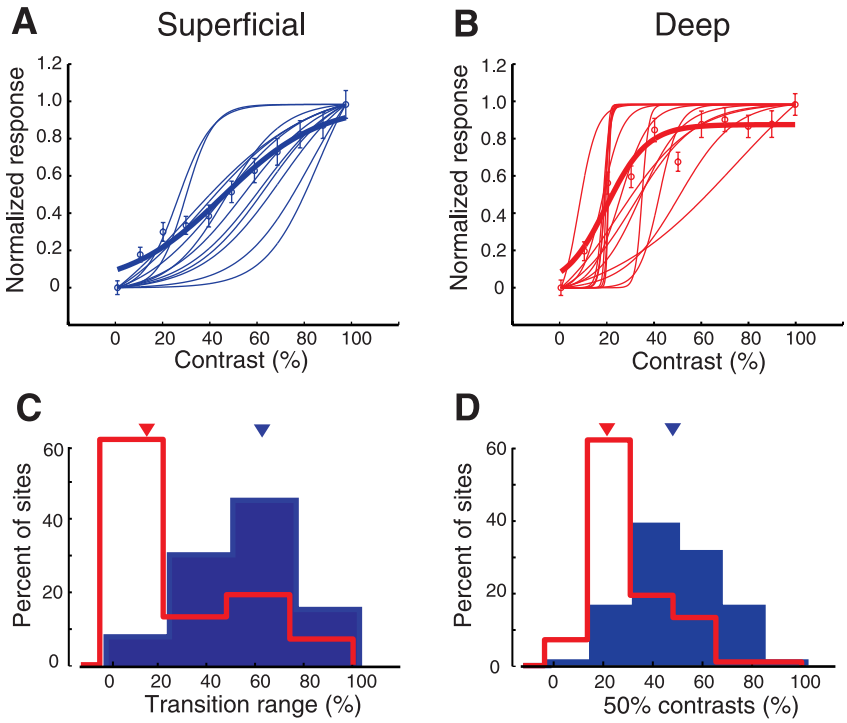

Fig. 7. Population summary of contrast-response functions for superficial and deep induced gamma LFP power. *A*: gamma LFP power at individual superficial layer sites (thin blue, sigmoidal fits) and the population mean (blue circles, and thick blue). Curves from individual sites were normalized to their maximum before averaging. Error bars show standard error of the mean across sites ($n = 13$). *B*: same as in *A* for deep layer sites ($n = 16$). *C*: distributions of gamma LFP power transition ranges for superficial (blue histogram) and deep (red histogram) sites. Inverted triangles: distribution medians. *D*: distributions of gamma LFP power 50% contrasts (the contrast at which gamma LFP power reached 50% of its maximum value) for superficial and deep sites. Other conventions are as in *C*.

We compared transition ranges and 50% contrast values for LFPs with those of spikes recorded at the same sites (Figs. 6 and 8). In the superficial layers, the distributions of transition ranges and 50% contrasts were similar for LFPs and spikes (Fig. 8, blue data; transition range: LFP = 60.9% [32.8−74.4%], spikes = 59.7% [54.2–77.1%], $P = 0.53$, $n = 13$; 50% contrast: LFP = 48.4% [39.9−66.4%], spikes = 55.2% [41.9–72.3%], $P = 0.93$, $n = 13$, Wilcoxon signed-rank test). In the deep layers, however, transition ranges for LFPs were on average about four times as sharp as those for spikes (Fig. 8A, red data; transition range: LFP = 17.4 [5.4−39.5] %, spikes = 68.3 [40.4−80.4] %, $P < 0.01$, $n = 16$, Wilcoxon signed rank test) and the 50% contrast values were shifted toward lower contrasts (Fig. 8*B*, red data; 50% contrast: LFP = 22.9% [18.7–34.0%], spikes = 46.6% [26.7–63.6%], $P < 0.001$, $n = 16$, Wilcoxon signed-rank test). The results were similar upon recomputing transition ranges and 50% contrasts on the basis of LFP rms amplitude. Thus, in the superficial layers, both LFP power and spike rates covaried over wide ranges of visual contrasts, whereas, in the deep layers, LFP power increased abruptly then remained constant while spike responses continued to encode increasing visual contrasts.

Temporal relationship of spikes with gamma oscillations. The LFP is a local phenomenon that cannot be detected, as such, by neurons downstream of the OT. On the other hand, synchronization of spikes to LFP phase, an indicator of synchronous spiking in networks of neurons (Fries et al. 2008), represents a synchrony code that could be detected by neurons downstream of the OT (Salinas and Sejnowski 2001; Tiesinga et al. 2008). Furthermore, the timing of spikes relative to LFP phase could carry information that could be read out by decoders local to the OT (O'Keefe and Recce 1993) or could be used to route information flow between the OT and its target nuclei (Sejnowski and Paulsen 2006; Womelsdorf et al. 2007).

To test whether spikes tended to synchronize with LFP phase, we measured spike-field coherence (SFC, MATERIALS AND METHODS). Visual stimuli presented in the center of the spike-receptive field induced SFC with a clear peak in the low-gamma band, for representative sites in both superficial and deep layers (Fig. 9, *A* and *B*). Population averages of the visually induced SFC are shown in Fig. 9*C* (superficial: blue, and deep: red), and population-averaged SFC induced by auditory stimuli is shown in Supplemental Fig. S4*A* (superficial: blue, and deep: red). Randomly matching spike times and

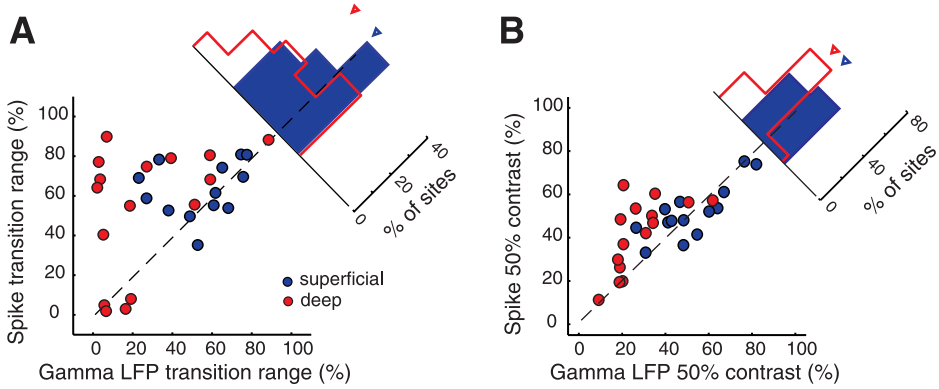

Fig. 8. Population summary comparing the contrast-response functions for induced gamma LFP and spikes. *A*: transition ranges for gamma LFP power (*x*-axis) and spike rates (*y*-axis) for superficial (blue, $n = 13$) and deep (red, $n = 16$) layer sites. The histogram shows the difference between spike and LFP transition ranges for the superficial and deep layer sites. Inverted triangle: distribution medians. Other conventions are as in Fig. 5. *B*: 50% contrast values for gamma LFP power (*x*-axis) and spike rates (*y*-axis) for superficial and deep layer sites. Other conventions are as in *A*.

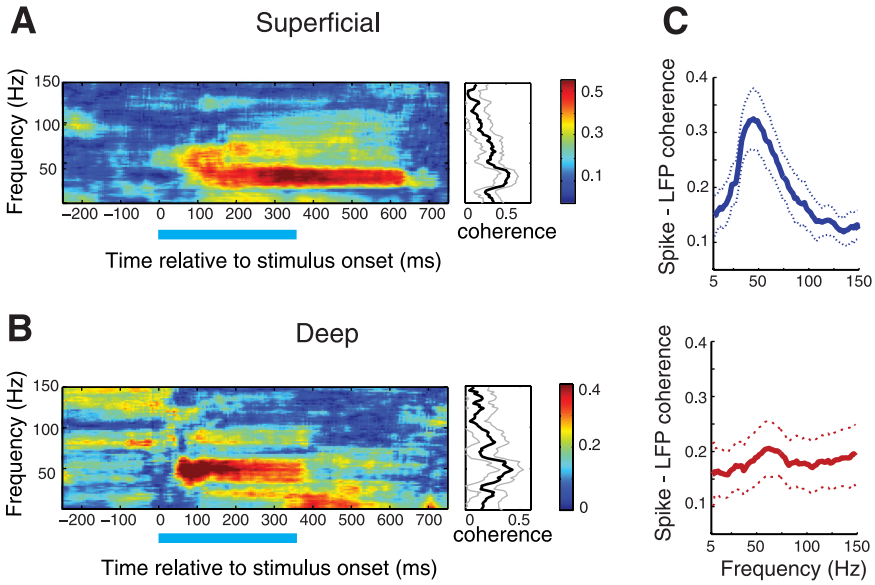

Fig. 9. Spike-field coherence in the superficial and deep layers. *A*: spike-field coherogram for an individual site in the superficial layers computed from responses to a visual stimulus (duration indicated by bar) at the center of the spike-receptive field. Color bar indicates coherence values. *Right*: coherence during stimulus presentation. Gray lines: 95% Jackknife confidence intervals. Other conventions are as in Fig. 2. *B*: same as in *A*, for an individual site in the deep layers. *C*: population average of the visually induced spike-field coherence in the superficial (blue, *top*), and deep (red, *bottom*) layers. Region between dotted lines: 95% confidence intervals across sites. Other conventions are as in Fig. 2.

LFPs across trials eliminated all coherence (Supplemental Fig. S4*B*), demonstrating that the spike-field coherence did not result from stimulus-locked oscillations in spikes and LFP.

Because we recorded spikes and LFPs from the same electrode, spike waveforms could contaminate LFPs, and the potential for spike contamination to affect SFC is greater in the high-gamma range (Zanos et al. 2011). Hence, we recomputed the population-averaged SFC, including only those sites at which SFC magnitude was greatest in the low-gamma (25–90 Hz) range. Visually evoked SFC magnitude was greatest in the low-gamma band (peak low-gamma SFC) in 92% (n = 23/25) of superficial, and 56% (n = 18/32) of deep layer sites. The average visually induced SFC across this subpopulation of sites is shown in Supplemental Fig. S4*C* (superficial: blue, and deep: red). Similarly, auditory stimuli evoked peak low-gamma SFC for 91% of superficial (n = 10/11) and 59% of deep (n = 10/17) layer sites (average SFC, Supplemental Fig. S4*D*). These results demonstrate that across a majority of superficial and deep layer sites, visual or auditory stimuli that were centered in the receptive field evoked neural firing that tended to synchronize with low-gamma LFP oscillations.

DISCUSSION

Our study describes gamma oscillations in the OT, the avian homolog of the SC, a midbrain structure that contributes to multimodal spatial localization, gaze control, and spatial attention (Butter et al. 1978; Olsen et al. 1989; Knudsen et al. 1993; Stein and Meredith 1993; Muller et al. 2005; McPeek and Keller 2004; Lovejoy and Krauzlis 2010). We observed that, when a single visual or auditory stimulus is presented to a tranquilized owl, the stimulus triggers strong gamma oscillations and spike-field coherence in the owl's OT across layers. Our results extend previous findings on the narrow tuning of gamma oscillations to stimulus features (Pesaran et al. 2002; Liu and Newsome 2006; Berens et al. 2008) and suggest that OT gamma oscillations carry precise spatial information that could contribute to the localization of sensory stimuli.

In our study, as in previous studies, spike times and LFPs were computed by differential filtering of signals recorded from the same electrode (Liu and Newsome 2006; Ray et al. 2008a; Xing et al. 2009; Chalk et al. 2010). The LFP is a reflection of synchronous transmembrane currents within a circumscribed volume of tissue. The main contribution to the LFP arises from synaptic potentials, rather than the rapid alternation of inward and outward currents associated with spikes (Buzsaki 2006). Thus LFP recordings made with low-impedance electrodes in the present study are likely to be dominated by synchronous network (synaptic) activity rather than by contributions from the spike waveforms. Although we cannot entirely exclude some contribution to the LFP, and SFC, from the depolarizing and hyperpolarizing after potentials associated with the spike, we interpolated out the spike waveform from the raw LFP signal in a ±2-ms window surrounding each spike to minimize this contribution. By quantitative analysis of the contribution of spike waveforms to LFP power, a previous study suggested that contamination by spike waveforms is greatest at frequencies above ~150 Hz (Colgin et al. 2009). In addition, a recent study that employed a mathematically rigorous framework for the removal of spike contamination from the LFP showed that visual tuning of the LFP was not strongly affected by spike contamination, even at high frequencies (up to 140 Hz, Zanos et al. 2011). Our analysis of LFP power and SFC included only the low-gamma band (25–90 Hz, as in Pesaran et al. 2002; Henrie and Shapley 2005; Katzner et al. 2009; Burns et al. 2010), even though we plotted frequencies up to 150 Hz (Pesaran et al. 2002; Colgin et al. 2009). Repeating these analyses in a more restricted frequency band (30–70 Hz, as in Traub et al. 1996; Traub et al. 2003; Vianney-Rodrigues et al. 2011) yielded similar results.

Gamma synchrony in the superficial layers. Spike-field coherence in the superficial layers was exceptionally strong in the low-gamma range. An important factor, unique to the superficial layers, must be considered when interpreting this result: whereas usually spike-field coherence is interpreted as an index of synchronization of postsynaptic (somatic) spikes to the LFP, spikes recorded in the superficial layers in our study likely included large-amplitude bursts that are generated by the axons of cholinergic neurons located in the nucleus Ipc (Fig. 10; adapted from Wang et al. 2006). In pigeons, intracellular

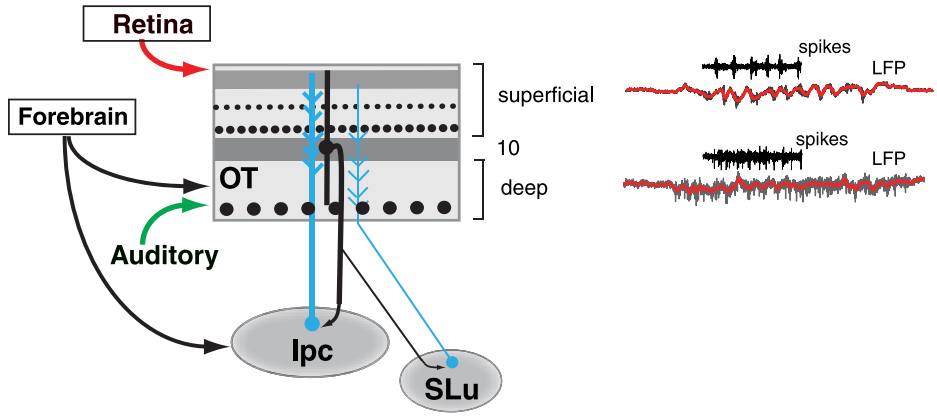

Fig. 10. Spike and LFP recordings in the context of the known connectivity of the midbrain tectoisthmic circuit. The superficial layers receive direct visual input from retinal afferents (red), but no direct auditory input from primary auditory structures. LFP oscillations in the superficial layers were prominent in the low-gamma range, and synchronized bursts recorded in these layers included putative axonal inputs from neurons in the adjoining nucleus isthmi pars parvocellularis (Ipc, blue). Ipc neurons, in turn, receive visual and auditory input from layer 10 of the OT (black), and provide bursting input with low-gamma periodicity to the superficial layers. The OT also receives input from the adjoining cholinergic nucleus semiluminaris (SLu, blue).

recordings from bursting units in the OT have identified the bursts as originating from axons of Ipc neurons (Marin et al. 2005). These axons have large diameters and form dense terminal fields of synaptic endings in the superficial layers, but not in the deep layers of the OT (Wang et al. 2006). In owls, extracellular recordings from the Ipc demonstrate that Ipc neurons have restricted, multimodal receptive fields and that they respond to either visual or auditory stimuli with periodic, synchronized bursts of spikes, the burst periodicity being in the low-gamma range (Maczko et al. 2006; Asadollahi et al. 2010). These properties are similar to those of the bursting spikes that we recorded in the superficial OT layers in this study. The large extracellular currents generated by these Ipc axon spikes in the superficial layers are difficult to exclude, particularly with low-impedance electrodes. These data suggest that our spike recordings in the superficial layers correspond, at least in part, to Ipc axon spikes.

We hypothesize that the periodic input from the Ipc to the superficial layers is largely responsible for the low-gamma oscillations in those layers. This hypothesis explains the observed similarities between spike responses and LFP-gamma power in spatial tuning and contrast-response functions in the superficial layers. The important implication of this hypothesis for the interpretation of spike-field coherence is that, rather than indicating the synchronization of somatic spikes to the LFP in the superficial layers (the usual interpretation), spike-field coherence in these layers reflects the synchrony between the Ipc spikes (input) and the LFP. Further experiments, in which somatic spikes are exclusively recorded in the superficial layers (with high-impedance electrodes) along with the LFP (recorded simultaneously with low-impedance electrodes), are necessary to determine whether there is, indeed, synchronization of postsynaptic unit responses in the superficial layers with the gamma oscillations of the LFP.

Gamma synchrony in the deep layers. The gamma oscillations that were evoked in the deep layers by either visual or auditory stimuli differed from those observed in the superficial layers; deep-layer oscillations showed broadly distributed induced power across the gamma-band. Such broadband gamma activity (encompassing 25–140 Hz) has been reported in the primate cortex (Henrie and Shapley 2005; Liu and Newsome 2006; Khayat et al. 2010; Ray et al. 2008b) and, recently, in the rodent hippocampus (Colgin et al. 2009). In addition, gamma power in the deep layers, unlike in the superficial layers, typically saturated at relatively low visual contrasts. Taken together with the observation that the neuroanatomy and physiology in the superficial and deep layers show distinctive properties (Fig. 10), this suggests that the mechanisms for generating LFP oscillations in the deep layers could be different from those that operate in the superficial layers. Specifically, the dominance of high-gamma power in the deeper layers suggests that oscillations in these layers could be driven by noisy interneuron networks intrinsic to the OT (Brunel and Wang 2003) or could engage distinct or additional elements in the OT microcircuit, such as the nucleus semiluminaris (SLu) that sends strong projections to the deep layers (Fig. 10).

Spike activity in the deep layers did not occur in bursts, and the spike waveforms were multiphasic, indicating that they represented somatic (postsynaptic) spikes. Hence, recordings from the deep layers were not contaminated by Ipc axon spikes. Therefore, spike-field coherence in the deep layers, indicative of the synchronization of somatic spikes (Fries et al. 2008), suggests that information is contained in spike synchrony, in addition to spike rate (Knudsen 1982). Such information encoded by synchronous, periodic discharges could be selectively decoded by neurons and circuits with resonant filtering properties downstream of the OT (Salinas and Sejnowski 2001; Tiesinga et al. 2008; Akam and Kullmann 2010).

Gamma oscillations are highly localized. Considerable controversy exists regarding the distance over which LFP currents spread (Katzner et al. 2009). In the mammalian cortex, LFP oscillations have been reported to spread across wide areas spanning several millimeters (Logothetis et al. 2001; Kreiman et al. 2006), implying that LFP spatial tuning should be broader than spike-rate spatial tuning. In contrast, we found that LFP spatial tuning in the OT is comparable to, and can be narrower than, spike-rate spatial tuning, consistent with the topographical, columnar organization of circuit elements in the OT. Our findings are in line with more recent physiological studies in the neocortex (Liu and Newsome 2006; Katzner et al. 2009; Xing et al. 2009) and models of gamma oscillations (Tiesinga and Buia 2009; Paik et al. 2009), indicating that LFP oscillations can represent input currents with high spatial resolution. In the OT, this corresponds to a high-resolution, topographic, mutimodal map of space.

Synchronous oscillatory input in the gamma-band has the potential to synchronize the firing of projection (pyramidal) neurons (Cardin et al. 2009). Indeed, we found that deep OT layer units synchronized with gamma oscillations when a stimulus was centered in the spike receptive field (Fig. 9, Supplemental Fig. S4, *A*, *C*, and *D*). Together with the highly

localized LFP oscillations in the deep layers, our findings indicate that the information contained in gamma synchronized spikes in the deep layers provides even higher spatial resolution than does the rate code. Sites with spike-rate spatial tuning exceeding 10°, characteristic of deep-layer projection neurons (Marin et al. 2003; Luksch 2003), exhibited narrower LFP spatial tuning. This result implies that gamma oscillations are weak on the flanks of these spike-receptive fields (Fig. 4*F*). Thus somatic spikes should only synchronize to the oscillations when stimuli are located near the center of the receptive field of the site. As a result, the spatial resolution of information contained in synchronized discharges would be substantially higher than that of information contained in spike rates near the center of the spike-receptive field.

On the other hand, spike rates discriminated adjacent stimuli more reliably (max d′) and exhibited higher Fisher information than did LFP power on the flanks of the spatial tuning curves. Fisher information depends on the change (derivative, or slope) of the conditional probability of the response across successive stimulus values (MATERIALS AND METHODS). In our recordings, the response level to stimuli at the receptive field center (peak) was 2.46 ± 0.14 (mean ± SE) times baseline for gamma LFP power (Fig. 3), and 10.54 ± 1.43 times baseline for spike rates (average across $n = 28$ superficial and $n = 42$ deep-layer sites). Thus, even though LFP tuning was narrower for deep-layer sites, tuning curve slopes were steeper for spike rates. Hence, the Fisher information and the d′ index, both of which depend on the slope of the tuning curve, were substantially higher for spike rates than for the LFPs, especially at the flanks of the tuning curves (Fig. 5, *C* and *D*, Supplemental Fig. S3). Taken together, these observations suggest the possibility that spike synchrony and spike rates provide complementary spatial information about stimuli in the center vs. flanks of the receptive field (Salinas and Sejnowski 2001; Niebur et al. 2002; Tiesinga et al. 2008).

Visual enhancement by multimodal gamma oscillations in the OT: a hypothesis. In our study, both visual and auditory stimuli evoked strong gamma oscillations in the superficial layers. The superficial layers of the OT in all classes of vertebrates are involved in the processing of visual information. Retinal ganglion cell axons and primary and secondary visual areas in the forebrain project directly to the superficial layers, and output neurons in the superficial layers project to visual nuclei in the thalamus and brainstem (Wild 1989; Luksch 2003; Berman and Wurtz 2010; Lyon et al. 2010). Neurons in the superficial layers respond vigorously and reliably to visual stimuli (Wurtz and Albano 1980). In contrast, there are no known inputs from (or outputs to) primarily auditory structures to (or from) the superficial layers. Moreover, lesions in the superficial layers result in visual deficits in tree shrews (Casagrande et al. 1972; Casagrande and Diamond 1974). What, then, is the origin of the auditory-driven oscillations in the superficial layers, and what function might these auditory-driven oscillations in the superficial layers serve?

Multimodal gamma oscillations in the superficial layers are likely to originate from the deep, multimodal OT layers. As discussed in a previous section, gamma oscillations in the superficial layers are tightly locked (coherent) with bursting spikes, which include, at least in part, bursting axonal spikes from cholinergic neurons in the Ipc (Marin et al. 2005). Ipc neurons, in turn, receive multimodal (visual and auditory) input from the OT by way of neurons in layer 10b, at the interface between the superficial and deep OT layers (Wang et al. 2006, black projection Fig. 10) and produce synchronized bursts at gamma frequencies (Maczko et al. 2006; Asadollahi et al. 2010). Thus sensory input (visual or auditory) that arrives in the deep OT layers drives gamma oscillations in the superficial layers via the Ipc (Fig. 10, blue).

Previous physiological and modeling studies have indicated that gamma oscillations can enhance the effectiveness of sensory input, synchronous input being more effective than rate-matched asynchronous input at driving neurons to spike (Tiesinga et al. 2004; Cardin et al. 2009). Thus superficial layer gamma oscillations, evoked by salient stimuli, could enhance the effectiveness of visual input to the OT. In addition, the synchronization of inputs can synchronize output spikes (measured here as SFC in the deep layers), which could increase the effectiveness of signaling to neurons downstream of the OT (Schoffelen et al. 2005). Because the auditory and visual receptive fields of neurons in the deep OT layers (and in the Ipc) are mutually aligned (Maczko et al. 2006; Wang et al. 2006), and because the oscillations tend to persist for roughly 100 ms after stimulus offset (Fig. 2), auditory-driven or visually driven gamma oscillations would enhance the processing of visual information from the same location in space. This mechanism could underlie spatial cueing effects wherein a salient auditory or visual stimulus enhances localization and detection of a subsequently presented visual stimulus at the same spatial location (Posner 1980). Moreover, because the frequency of gamma oscillations and coherence does not appear to vary substantially with stimulus modality (Figs. 2–3, Supplemental Fig. S4) or contrast (Fig. 6), the oscillations could act as a communication channel for enhanced transmission of information from the OT to downstream regions (Fries 2005; Womelsdorf et al. 2007).

Modulation of stimulus-evoked gamma LFP power is a hallmark of attention in the mammalian neocortex (Fries et al. 2001). The precise interplay between the OT and the isthmic complex in generating gamma oscillations in the avian midbrain, and the role of these tectal oscillations in multisensory processing, spatial localization, and spatial attention, are issues that are fundamental to understanding how these processes work across species and across brain structures.

ACKNOWLEDGMENTS

We thank Ali Asadollahi, Catherine Dunn, Alex Goddard, and Shreesh Mysore for their comments on a preliminary version of the manuscript, and Phyllis Knudsen for assistance with preparing figures. D. Sridharan thanks Shreesh Mysore and Ali Asadollahi for help and guidance with owl surgical procedures, and Shreesh Mysore and Phyllis Knudsen for help with the lesion reconstructions.

GRANTS

This research was supported by The NIH Director's Pioneer Award DP1-OD000965 (K. Boahen) and National Institutes of Health Grant 9R01 EY019179-29 (E. Knudsen).

DISCLOSURES

No conflicts of interest, financial or otherwise, are declared by the authors.

REFERENCES

Akam T, Kullmann DM. Oscillations and filtering networks support flexible routing of information. *Neuron* 67: 308–320, 2010.

Asadollahi A, Mysore SP, Knudsen EI. Stimulus-driven competition in a cholinergic midbrain nucleus. *Nat Neurosci* 13: 889–895, 2010.

Bala AD, Spitzer MW, Takahashi TT. Auditory spatial acuity approximates the resolving power of space-specific neurons. *PLos One* 2: e675, 2007.

Bala AD, Spitzer MW, Takahashi TT. Prediction of auditory spatial acuity from neural images on the owl's auditory space map. *Nature* 424: 771–774, 2003.

Berens P, Keliris GA, Ecker AS, Logothetis NK, Tolias AS. Comparing the feature selectivity of the gamma-band of the local field potential and the underlying spiking activity in primate visual cortex (Abstract). *Front Syst Neurosci* 2: 2, 2008.

Berman RA, Wurtz RH. Functional identification of a pulvinar path from superior colliculus to cortical area MT. *J Neurosci* 30: 6342–6354, 2010.

Bravo H, Pettigrew JD. The distribution of neurons projecting from the retina and visual cortex to the thalamus and tectum opticum of the barn owl, Tyto alba, and the burrowing owl, Speotyto cunicularia. *J Comp Neurol* 199: 419–441, 1981.

Brecht M, Goebel R, Singer W, Engel AK. Synchronization of visual responses in the superior colliculus of awake cats. *Neuroreport* 12: 43–47, 2001.

Brosch M, Budinger E, Scheich H. Stimulus-related gamma oscillations in primate auditory cortex. *J Neurophysiol* 87: 2715–2725, 2002.

Brunel N, Wang XJ. What determines the frequency of fast network oscillations with irregular neural discharges? I. Synaptic dynamics and excitation-inhibition balance. *J Neurophysiol* 90: 415–430, 2003.

Burns SP, Xing D, Shapley RM. Comparisons of the dynamics of local field potential and multiunit activity signals in macaque visual cortex. *J Neurosci* 30: 13739–13749, 2010.

Butter CM, Weinstein C, Bender DB, Gross CG. Localization and detection of visual stimuli following superior colliculus lesions in rhesus monkeys. *Brain Res* 156: 33–49, 1978.

Buzsaki G, Horvath Z, Urioste R, Hetke J, Wise K. High-frequency network oscillation in the hippocampus. *Science* 256: 1025–1027, 1992.

Buzsaki G. *Rhythms of the Brain.* New York: Oxford University Press, 2006, p. 89–92.

Canolty RT, Edwards E, Dalal SS, Soltani M, Nagarajan SS, Kirsch HE, Berger MS, Barbaro NM, Knight RT. High gamma power is phase-locked to theta oscillations in human neocortex. *Science* 313: 1626–1628, 2006.

Cardin JA, Carlen M, Meletis K, Knoblich U, Zhang F, Deisseroth K, Tsai LH, Moore CI. Driving fast-spiking cells induces gamma rhythm and controls sensory responses. *Nature* 459: 663–667, 2009.

Casagrande VA, Diamond IT. Ablation study of the superior colliculus in the tree shrew (Tupaia glis). *J Comp Neurol* 156: 207–237, 1974.

Casagrande VA, Harting JK, Hall WC, Diamond IT, Martin GF. Superior colliculus of the tree shrew: a structural and functional subdivision into superficial and deep layers. *Science* 177: 444–447, 1972.

Chalk M, Herrero JL, Gieselmann MA, Delicato LS, Gotthardt S, Thiele A. Attention reduces stimulus-driven gamma frequency oscillations and spike field coherence in V1. *Neuron* 66: 114–125, 2010.

Colgin LL, Denninger T, Fyhn M, Hafting T, Bonnevie T, Jensen O, Moser MB, Moser EI. Frequency of gamma oscillations routes flow of information in the hippocampus. *Nature* 462: 353–357, 2009.

DeBello WM, Knudsen EI. Multiple sites of adaptive plasticity in the owl's auditory localization pathway. *J Neurosci* 24: 6853–6861, 2004.

Fedtsova N, Quina LA, Wang S, Turner EE. Regulation of the development of tectal neurons and their projections by transcription factors Brn3a and Pax7. *Dev Biol* 316: 6–20, 2008.

Fries P. A mechanism for cognitive dynamics: neuronal communication through neuronal coherence. *Trends Cogn Sci* 9: 474–480, 2005.

Fries P, Reynolds JH, Rorie AE, Desimone R. Modulation of oscillatory neuronal synchronization by selective visual attention. *Science* 291: 1560–1563, 2001.

Fries P, Womelsdorf T, Oostenveld R, Desimone R. The effects of visual stimulation and selective visual attention on rhythmic neuronal synchronization in macaque area V4. *J Neurosci* 28: 4823–4835, 2008.

Gregoriou GG, Gotts SJ, Zhou H, Desimone R. High-frequency, long-range coupling between prefrontal and visual cortex during attention. *Science* 324: 1207–1210, 2009.

Henrie JA, Shapley R. LFP power spectra in V1 cortex: the graded effect of stimulus contrast. *J Neurophysiol* 94: 479–490, 2005.

Karten HJ, Cox K, Mpodozis J. Two distinct populations of tectal neurons have unique connections within the retinotectorotundal pathway of the pigeon (Columba livia). *J Comp Neurol* 387: 449–465, 1997.

Karten HJ, Hodos W, Nauta WJ, Revzin AM. Neural connections of the "visual wulst" of the avian telencephalon. Experimental studies in the pigeon (Columba livia) and owl (Speotyto cunicularia). *J Comp Neurol* 150: 253–278, 1973.

Katzner S, Nauhaus I, Benucci A, Bonin V, Ringach DL, Carandini M. Local origin of field potentials in visual cortex. *Neuron* 61: 35–41, 2009.

Kayser C, Konig P. Stimulus locking and feature selectivity prevail in complementary frequency ranges of V1 local field potentials. *Eur J Neurosci* 19: 485–489, 2004.

Khawaja FA, Tsui JM, Pack CC. Pattern motion selectivity of spiking outputs and local field potentials in macaque visual cortex. *J Neurosci* 29: 13702–13709, 2009.

Khayat PS, Niebergall R, Martinez-Trujillo JC. Frequency-dependent attentional modulation of local field potential signals in macaque area MT. *J Neurosci* 30: 7037–7048, 2010.

Knudsen EI. Auditory and visual maps of space in the optic tectum of the owl. *J Neurosci* 2: 1177–1194, 1982.

Knudsen EI, Knudsen PF, Masino T. Parallel pathways mediating both sound localization and gaze control in the forebrain and midbrain of the barn owl. *J Neurosci* 13: 2837–2852, 1993.

Kreiman G, Hung CP, Kraskov A, Quiroga RQ, Poggio T, DiCarlo JJ. Object selectivity of local field potentials and spikes in the macaque inferior temporal cortex. *Neuron* 49: 433–445, 2006.

Liu J, Newsome WT. Local field potential in cortical area MT: stimulus tuning and behavioral correlations. *J Neurosci* 26: 7779–7790, 2006.

Logothetis NK, Pauls J, Augath M, Trinath T, Oeltermann A. Neurophysiological investigation of the basis of the fMRI signal. *Nature* 412: 150–157, 2001.

Lovejoy LP, Krauzlis RJ. Inactivation of primate superior colliculus impairs covert selection of signals for perceptual judgments. *Nat Neurosci* 13: 261–266, 2010.

Luksch H. Cytoarchitecture of the avian optic tectum: neuronal substrate for cellular computation. *Rev Neurosci* 14: 85–106, 2003.

Lyon DC, Nassi JJ, Callaway EM. A disynaptic relay from superior colliculus to dorsal stream visual cortex in macaque monkey. *Neuron* 65: 270–279, 2010.

Maczko KA, Knudsen PF, Knudsen EI. Auditory and visual space maps in the cholinergic nucleus isthmi pars parvocellularis of the barn owl. *J Neurosci* 26: 12799–12806, 2006.

Manning JR, Jacobs J, Fried I, Kahana MJ. Broadband shifts in local field potential power spectra are correlated with single-neuron spiking in humans. *J Neurosci* 29: 13613–13620, 2009.

Marin G, Letelier JC, Henny P, Sentis E, Farfan G, Fredes F, Pohl N, Karten H, Mpodozis J. Spatial organization of the pigeon tectorotundal pathway: an interdigitating topographic arrangement. *J Comp Neurol* 458: 361–380, 2003.

Marin G, Mpodozis J, Sentis E, Ossandon T, Letelier JC. Oscillatory bursts in the optic tectum of birds represent re-entrant signals from the nucleus isthmi pars parvocellularis. *J Neurosci* 25: 7081–7089, 2005.

May PJ. The mammalian superior colliculus: laminar structure and connections. *Prog Brain Res* 151: 321–378, 2006.

McPeek RM, Keller EL. Deficits in saccade target selection after inactivation of superior colliculus. *Nat Neurosci* 7: 757–763, 2004.

Middlebrooks JC, Knudsen EI. A neural code for auditory space in the cat's superior colliculus. *J Neurosci* 4: 2621–2634, 1984.

Mitra P, Bokil H. *Observed Brain Dynamics*. New York: Oxford University Press, 2008.

Muller JR, Philiastides MG, Newsome WT. Microstimulation of the superior colliculus focuses attention without moving the eyes. *Proc Natl Acad Sci USA* 102: 524–529, 2005.

Mysore SP, Asadollahi A, Knudsen EI. Global inhibition and stimulus competition in the owl optic tectum. *J Neurosci* 30: 1727–1738, 2010.

Neuenschwander S, Varela FJ. Visually triggered neuronal oscillations in the pigeon: an autocorrelation study of tectal activity. *Eur J Neurosci* 5: 870–881, 1993.

Niebur E, Hsiao SS, Johnson KO. Synchrony: a neuronal mechanism for attentional selection? *Curr Opin Neurobiol* 12: 190–194, 2002.

O'Keefe J, Recce ML. Phase relationship between hippocampal place units and the EEG theta rhythm. *Hippocampus* 3: 317–330, 1993.

Olsen JF, Knudsen EI, Esterly SD. Neural maps of interaural time and intensity differences in the optic tectum of the barn owl. *J Neurosci* 9: 2591–2605, 1989.

Paik SB, Kumar T, Glaser DA. Spontaneous local gamma oscillation selectively enhances neural network responsiveness. *PLoS Comput Biol* 5: e1000342, 2009.

Pesaran B, Pezaris JS, Sahani M, Mitra PP, Andersen RA. Temporal structure in neuronal activity during working memory in macaque parietal cortex. *Nat Neurosci* 5: 805–811, 2002.

Posner MI. Orienting of attention. *Q J Exp Psychol B* 32: 3–25, 1980.

Quian Quiroga R, Panzeri S. Extracting information from neuronal populations: information theory and decoding approaches. *Nat Rev Neurosci* 10: 173–185, 2009.

Raczkowski D, Casagrande VA, Diamond IT. Visual neglect in the tree shrew after interruption of the descending projections of the deep superior colliculus. *Exp Neurol* 50: 14–29, 1976.

Ray S, Crone NE, Niebur E, Franaszczuk PJ, Hsiao SS. Neural correlates of high-gamma oscillations (60–200 Hz) in macaque local field potentials and their potential implications in electrocorticography. *J Neurosci* 28: 11526–11536, 2008a.

Ray S, Hsiao SS, Crone NE, Franaszczuk PJ, Niebur E. Effect of stimulus intensity on the spike-local field potential relationship in the secondary somatosensory cortex. *J Neurosci* 28: 7334–7343, 2008b.

Sakitt B. Indices of discriminability. *Nature* 241: 133–134, 1973.

Salinas E, Sejnowski TJ. Correlated neuronal activity and the flow of neural information. *Nat Rev Neurosci* 2: 539–550, 2001.

Schoffelen JM, Oostenveld R, Fries P. Neuronal coherence as a mechanism of effective corticospinal interaction. *Science* 308: 111–113, 2005.

Sejnowski TJ, Paulsen O. Network oscillations: emerging computational principles. *J Neurosci* 26: 1673–1676, 2006.

Seung HS, Sompolinsky H. Simple models for reading neuronal population codes. *Proc Natl Acad Sci USA* 90: 10749–10753, 1993.

Sohal VS, Zhang F, Yizhar O, Deisseroth K. Parvalbumin neurons and gamma rhythms enhance cortical circuit performance. *Nature* 459: 698–702, 2009.

Stein BE, Meredith MA. *The Merging of the Senses*. Cambridge, MA: The MIT Press, Cambridge, 1993.

Tiesinga PH, Buia CI. Spatial attention in area V4 is mediated by circuits in primary visual cortex. *Neural Netw* 22: 1039–1054, 2009.

Tiesinga P, Fellous JM, Sejnowski TJ. Regulation of spike timing in visual cortical circuits. *Nat Rev Neurosci* 9: 97–107, 2008.

Tiesinga PH, Fellous JM, Salinas E, Jose JV, Sejnowski TJ. Inhibitory synchrony as a mechanism for attentional gain modulation. *J Physiol (Paris)* 98: 296–314, 2004.

Traub RD, Cunningham MO, Gloveli T, LeBeau FE, Bibbig A, Buhl EH, Whittington MA. GABA-enhanced collective behavior in neuronal axons underlies persistent gamma-frequency oscillations. *Proc Natl Acad Sci USA* 100: 11047–11052, 2003.

Traub RD, Jefferys JG, Whittington MA. *Fast Oscillations in Cortical Circuits*. Cambridge, MA: The MIT Press, Cambridge, 1999a.

Traub RD, Schmitz D, Jefferys JG, Draguhn A. High-frequency population oscillations are predicted to occur in hippocampal pyramidal neuronal networks interconnected by axoaxonal gap junctions. *Neuroscience* 92: 407–426, 1999b.

Traub RD, Whittington MA, Stanford IM, Jefferys JG. A mechanism for generation of long-range synchronous fast oscillations in the cortex. *Nature* 383: 621–624, 1996.

Vianney-Rodrigues P, Iancu OD, Welsh JP. Gamma oscillations in the auditory cortex of awake rats. *Eur J Neurosci* 33: 119–129, 2011.

Wang Y, Luksch H, Brecha NC, Karten HJ. Columnar projections from the cholinergic nucleus isthmi to the optic tectum in chicks (Gallus gallus): a possible substrate for synchronizing tectal channels. *J Comp Neurol* 494: 7–35, 2006.

Wild JM. Pretectal and tectal projections to the homologue of the dorsal lateral geniculate nucleus in the pigeon: an anterograde and retrograde tracing study with cholera toxin conjugated to horseradish peroxidase. *Brain Res* 479: 130–137, 1989.

Winkowski DE, Knudsen EI. Distinct mechanisms for top-down control of neural gain and sensitivity in the owl optic tectum. *Neuron* 60: 698–708, 2008.

Winkowski DE, Knudsen EI. Top-down control of multimodal sensitivity in the barn owl optic tectum. *J Neurosci* 27: 13279–13291, 2007.

Winkowski DE, Knudsen EI. Top-down gain control of the auditory space map by gaze control circuitry in the barn owl. *Nature* 439: 336–339, 2006.

Witten IB, Knudsen PF, Knudsen EI. A dominance hierarchy of auditory spatial cues in barn owls. *PLos One* 5: e10396, 2010.

Womelsdorf T, Schoffelen JM, Oostenveld R, Singer W, Desimone R, Engel AK, Fries P. Modulation of neuronal interactions through neuronal synchronization. *Science* 316: 1609–1612, 2007.

Wurtz RH, Albano JE. Visual-motor function of the primate superior colliculus. *Annu Rev Neurosci* 3: 189–226, 1980.

Xing D, Yeh CI, Shapley RM. Spatial spread of the local field potential and its laminar variation in visual cortex. *J Neurosci* 29: 11540–11549, 2009.

Zanos TP, Mineault PJ, Pack CC. Removal of spurious correlations between spikes and local field potentials. *J Neurophysiol* 105: 474–486, 2011.